

Eliminating object prior-bias from sparse-projection tomographic reconstructions

Preeti Gopal, Sharat Chandran, Imants Svalbe, and Ajit Rajwade

Abstract—Tomographic reconstruction from undersampled measurements is a necessity when the measurement process is potentially harmful, needs to be rapid, or is resource-expensive. In such cases, information from previously existing longitudinal scans of the same object ('object-prior'), helps in the reconstruction from the current measurements of that object ('test'), while requiring significantly fewer updating measurements. In this work, we improve the state of the art by proposing the context under which priors can be effectively used based on the final goal of the application at hand.

Our work is based on longitudinal data acquisition scenarios where we wish to study new changes that evolve within an object over time, such as in repeated scanning for disease monitoring, or in tomography-guided surgical procedures. While this is easily feasible when measurements are acquired from a large number of projection angles ('views'), it is challenging when the number of views is limited.

If the goal is to track the changes while simultaneously reducing sub-sampling artefacts, we propose (1) acquiring measurements from an *extremely small* number of views and using a 'uniform' prior-based reconstruction. If the goal is to observe details of new changes, we propose (2) acquiring measurements from a *moderate* number of views (albeit, still sub-Nyquist), and using a more involved reconstruction routine. We show that in the latter case, a 'spatially-varying' technique is appropriate in order to prevent the prior from adversely affecting the reconstruction of new structures that are absent in any of the earlier scans. The reconstruction of new regions is safeguarded from the bias of the prior by computing regional weights that moderate the local influence of the priors. We are thus able to effectively reconstruct both the old and the new structures in the test. We have tested the efficacy of our method on synthetic as well as real projection data. The results demonstrate the use of both uniform and spatially-varying priors in different scenarios. Our methods significantly improve the overall quality of the reconstructed data while minimizing the number of measurements needed for imaging in longitudinal studies.

Index Terms—Limited-view tomographic reconstruction, compressed sensing, priors, longitudinal studies.

I. INTRODUCTION

Computed Tomography (CT) deals with the recovery of details of an object's interior from a limited set of projection data acquired by passing X-rays at different orientations ('views'). It is preferable to minimize the radiation exposed in order to prevent any potential damage to it and in order to reduce the acquisition time. Therefore, current research seeks to either significantly reduce the radiation intensity

Preeti Gopal is with IITB-Monash Research Academy

Sharat Chandran and Ajit Rajwade are with the Department of Computer Science and Engineering, IIT Bombay

Imants Svalbe is with the School of Physics and Astronomy, Monash University

required to reconstruct with adequate fidelity [1], [2], [3], [4] or significantly reduce the number of measurements required to reconstruct with adequate fidelity. For the latter case, there are two lines of pursuit. One is to intelligently choose those sets of projection views that capture most information [5], [6], [7], [8], [9], and the other, which is the focus of this paper, is to design the reconstruction algorithm in order to achieve the most accurate recovery of the underlying slice, given the measurements from any limited set of views [1], [10], [11].

In conventional data acquisition techniques, the tomographic measurements \mathbf{y} are acquired by sampling the physical object \mathbf{x} uniformly with a substantial number of views, ideally above the Nyquist rate. In such a case when there are sufficient measurements, reconstruction using the conventional filtered backprojection (FBP) suffices, as seen in Fig. 1 (first column, 600 views). The figure shows the ground truth image (260×260) of naturally growing sprouts at the top left (the details of this dataset is postponed to Section VII).

However, in the last decade, reconstruction from reduced views has been made possible by assuming the data to exhibit sparsity under certain mathematical transforms Υ such as the wavelet transforms, or the Discrete Cosine Transform (DCT). This is known as sparsity prior and is the fundamental principle in the widely used Compressed Sensing (CS) technique [12], [13]. There are multiple ways to incorporate the sparsity prior using CS. We use the LASSO (least absolute shrinkage and selection operator) which iteratively solves for the solution by penalizing a combination of least squares error and L_1 -norm of the sparse coefficients θ of the object \mathbf{x} . If Ψ represents the sparsity basis, i.e., if $\mathbf{x} = \Psi\theta$, and \mathcal{R} represents the acquisition model, then the LASSO solution is described by one that minimizes

$$J_{\text{CS}}(\theta) = \|\mathcal{R}\Psi\theta - \mathbf{y}\|_2^2 + \lambda_1\|\theta\|_1. \quad (1)$$

Fig. 1 (second column) demonstrates the benefit of using sparsity prior when the number of projection views is limited (100 views). We solve this cost function using the popular l_1 -regularized least squares (l_1 -ls) package available in [14], and choose DCT as our sparsity basis Υ . We had observed no significant improvement if, say, the wavelet transform were instead used as the basis.

When the number of views is significantly reduced (this paper), the sparsity prior alone is not sufficient. In such cases additional information ('object-prior') specific to the current object being scanned (called the 'test' henceforth) is useful in further improving the reconstruction. While this has been done in the context of dynamic CT-scans (discussed more in Section II), in this paper we use a set S of previous scans of

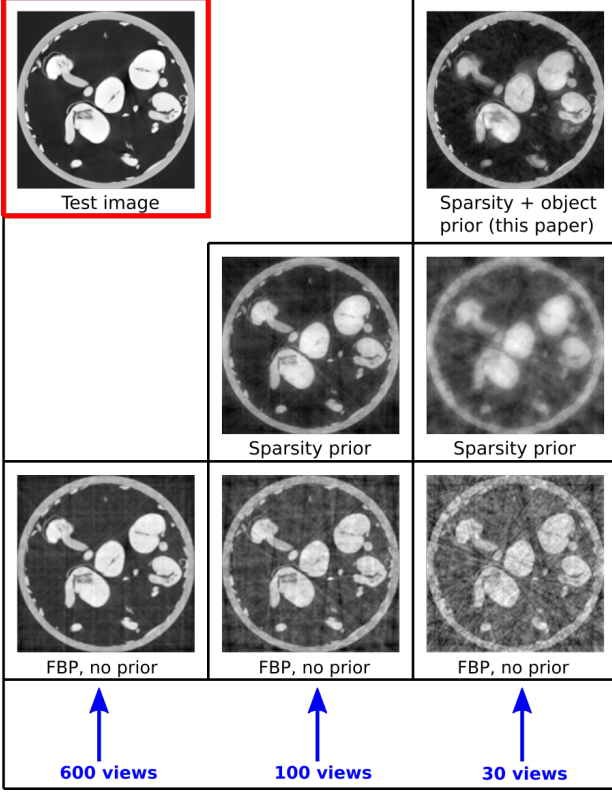


Fig. 1: Illustration of the use of various priors in the reconstruction reduces the number of views. In all cases, the ground truth (260×260) appears in the top left. For extremely large number of views (600 views), the FBP reconstruction (first column) is of very good quality (Structural Similarity Index Metric, SSIM=0.92). As the number of views become limited (100 views), the reconstruction using sparsity prior (middle column) is better both visually and quantitatively than FBP (SSIM of 0.90 vs 0.83). If the number of views is drastically reduced (30 views), the presence of both sparsity prior and object prior improves the reconstruction (SSIM=0.85) when compared to presence of only sparsity prior (SSIM=0.82) or no prior (SSIM=0.69).

the same object. This is relevant in a longitudinal context: the acquisition of sequential CT scans of the same subject in order to track time-evolving changes within the subject's interior. As seen in Fig. 1 (last column, 30 views) our method uses the set S uniformly by creating an eigenspace representation (Section VI).

However, with the use of such an object prior, a new challenge emerges. The prior set S may potentially overwhelm the necessary details, and when several prior scans are available, finding the right prior is an issue. We therefore seek an algorithm that estimates the location and magnitude of new changes in the (unknown) test. As we show in Section VIII, this eventually prevents the prior from adversely affecting the reconstruction of new regions in the test. We refer to this method as a *spatially-varying* prior-based reconstruction routine, that still uses *all* the previous scans in the set S , without using simply the prior scan, or endeavoring to find the “right” prior.

This paper is organized as follows. After discussing related work in Section II, Section III lays down the key contributions of this work. Details of the datasets created and used for

validation are described in Section IV. Section V demonstrates the utility of both the uniform and spatially-varying methods on a longitudinal medical dataset. We now move to the details. Section VI describes the construction of the uniform eigenspace prior, followed by the corresponding results in real and synthetic 3D biological datasets in Section VII. Section VIII describes how the uniform prior needs to be modified when accurate details of new changes are to be observed. A spatially-varying technique offers a solution, the results of which are presented in Section IX. Section X discusses tuning of the hyperparameters involved, and limitations of our method. Finally, we conclude with key inferences that can be drawn from our work in Section XI.

II. RELATED WORK

The idea of using a reduced number of views is most pronounced in specialized applications. For example, in [15], sparsity-constrained optimization is presented for angiography. Here, the regions of interest are the vessels alone and they are highlighted by physically inserting a contrast agent, and therefore there is an inherent sharper contrast between the vessels and the background. In other applications where the spatial-gradient of the underlying volume is known to be sparse, the ‘total variation’ method, as used in [16], [17], can be applied. In a more generalized application scenario, like the ones addressed in this paper, any information about the regions of interest is not known, and such techniques have limited applicability.

Most object-prior based reconstruction have been in the areas of dynamic CT and 4D-CT. The object-prior usually consists of an object reconstructed to high quality from a large number of projection angles. One of the earliest pieces of work in this area is the well-cited PICCS method [18] for dynamic CT, which enforces a robust-norm based similarity between the test and the object prior, in addition to a sparsity prior on the test. The limitation is the unchecked over-emphasis of the prior on the reconstruction of the test at hand. A closely related method called PIRPLE was proposed in [19], with additional steps to register the object prior and the test and a somewhat more flexible combination of data fidelity terms, sparsity prior and object prior. However, this method too has similar limitations as PICCS.

In order to prevent the object-prior from overwhelming the reconstruction of test, a few other approaches have either estimated the motion between the object-prior and the test or have applied very specific object-properties for identifying the new changes in the test. Examples for the former include [20], where the changes across the successive scan volumes are assumed to be continuous, thus enabling the use of optical flow to model the motion between corresponding voxels of different scan volumes. In another study [21], changes between successive scans were modelled by affine deformation whose parameters were computed for motion-correction, which in turn enables acquisition from fewer views. In [22], all the scan volumes are reconstructed together using spatio-temporal regularization. Here again, the inherent assumption is the continuity across volumes in space or time.

The methods that use object-specific knowledge are [23] and [24]. In [23], the knowledge of the attenuation coefficient of the fluid is used as a prior for reconstructing its flow through gravel. However, this relies on additional expert domain knowledge which may not be available or which may be infeasible to acquire. Other approaches variously use robust principal components analysis assuming that the object consists of a large static part (background) and a sparse moving part (foreground) [25], spline-based models for tracking the regions of change in an SIRT framework [26].

However, all these techniques [22], [20], [23], [25], [26] essentially reconstruct all the different stages of the object simultaneously, and use the extra redundancy across time simultaneously. In the scenario of a longitudinal study (where projection measurements are acquired at instants that are several weeks apart) which we consider in this paper, such approaches are not feasible. A longitudinal study will necessarily require reconstruction results after acquisition of each set of measurements.

There exists methods for estimating the new changes (in the test) directly in the projection space. In such techniques which can be used in longitudinal studies, the object prior is projected in the same set of views as the current set of test measurements, and a set of projection differences is computed. These projection differences are essentially tomographic projections of the difference between the unknown test and the known object prior. Hence, a variety of reconstruction algorithms can be used to estimate such a difference image which can then be added to the object prior to yield the final estimate of the test. Such methods have been proposed in [27], [28]. However, the reconstruction of the difference image will inherently contain sub-sampling artefacts, and these artefacts will appear in the final reconstruction as there is no mechanism to mitigate them (unlike the method that we propose). This can be seen in Sec. 4 of our supplementary material [29], where we have compared our method with [28].

In this paper, we present a technique that makes use of multiple object priors, corresponding to high quality reconstructions of similar objects across time, typically in a longitudinal study. We use these priors to improve the reconstruction of the test from largely undersampled measurements. In particular, we define the regions of change between the test and the eigenspace spanned by the previous high quality object priors in a purely data driven manner. Additionally, our technique differentiates between genuine structural changes and “changes” that appear due to undersampling artefacts (as seen in Sec. 4 of our supplementary material [29]). Besides this, since we use a statistical model with multiple object priors, we avoid the problem of selecting an appropriate single object prior unlike [18], [27], [28], [19], [24] and also make use of the additional information available in the multiple priors. Our technique also has the advantage of not requiring any expert-domain knowledge about the object being scanned.

III. CONTRIBUTIONS

This paper focusses on few-views reconstruction with an emphasis on longitudinal studies. In contrast to the object

prior-based studies mentioned above, we reconstruct the current test object without any assumption of continuity of changes or some knowledge of the attenuation coefficients of the structures. We do not make any temporal assumption in terms of time intervals – prior scans could be months apart. We use the current measurements from few-views and previous scans of the same object. A key idea in our work is the starting point – the new test volume is close to the space spanned by the eigenvectors of the multiple representative previously scanned objects.

We also demonstrate how the uniform prior can impose an inflexible constant weight (and hence an unnecessary bias) when reconstructing the data. As a solution, we present a method to moderate the control of the prior by estimating and imposing spatially-varying weights to the prior in order to reconstruct new structures accurately. This spatially-varying prior tunes the effect of the templates in different regions of the reconstruction.

Fig. 2 provides an overview.

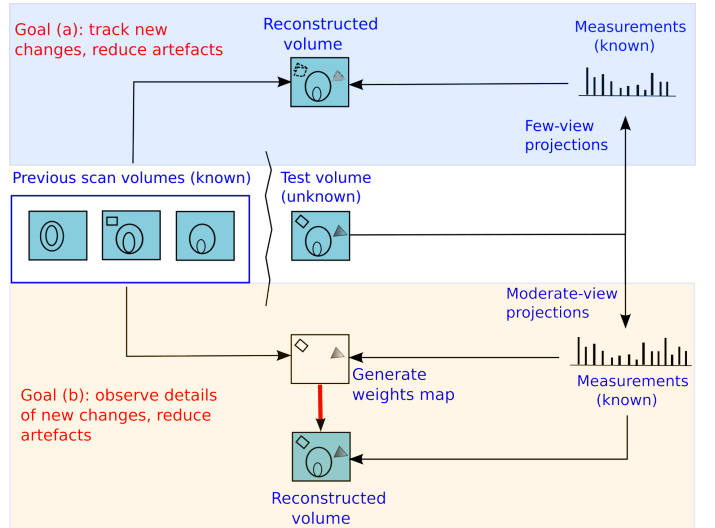


Fig. 2: Overview of our work. The choice of the number of measurement views and the type of reconstruction is driven by the goal in the application under consideration. (a) When our goal is relatively simple, such as tracking the location of new changes while simultaneously reducing sub-sampling artefacts, we propose acquiring measurements from an extremely small number of views ('few-view' imaging) and using uniform prior based reconstruction. (b) When our goal becomes more ambitious, such as observing details of the new changes while simultaneously reducing sub-sampling artefacts, we propose acquiring measurements from a slightly higher number of views ('moderate-view' imaging) and using spatially-varying prior-based reconstruction. In either case, the number of views is lower than what is conventionally used.

In summary, the key contributions are

- We create new 3D biological datasets (Section IV) and present results on real cone-beam projections. Our datasets and code will be made available to the community.
- As seen in Fig. 1, we demonstrate the use of uniform priors when very few views are used. More results appear in Section VII and in the supplementary material.

- We discuss the scenarios where a uniform object prior is sufficient for the application at hand, and the scenarios for which it will fail. This leads to the idea of a weights map designed to depict the location and strength of new changes at every voxel. A novel algorithm is presented to build this map from sub-sampled measurements of the test and a set of high quality templates. Once the weights map is built, it is used for accurate reconstruction of those changes in the test that are absent in all of the templates. Results appear in Section IX.
- We show the efficacy of our results in a real-life medical longitudinal studies with data obtained in a clinical setting from a live teaching and research hospital

IV. DATASETS

In this section, we lay the details of all the real and simulated datasets created and used for this work. The first 3 datasets: Okra, Potato and Sprouts were acquired from the Australian National University (ANU). We wish to emphasize that data from commercially available CT machines may not be suitable because most CT scanners do not reveal the raw measurements, and instead output only the full reconstructed volumes. Moreover, the process of conversion from the projections to the full volumes is proprietary. Departing from this, we demonstrate reconstruction results (in Sections VII and IX) from the following datasets.

Okra: This dataset is that of an Okra specimen consisting of its five scans (Fig. 3). Prior to the first scan, two cuts were drilled on the surface of the specimen. This was followed by four scans, each after introducing one new cut. The specimen was kept in the same position throughout the acquisitions. The measurements consisted of real circular cone-beam projections from 450 views, each of size 336×156 . In our experiments, the first 4 volumes shown in Fig. 3 were used to build the object-prior and the last volume was used as the test. The ground truth consists of volumes of size $338 \times 338 \times 123$ reconstructed using the Feldkamp-Davis-Kress (FDK) algorithm [30] from the full set of 450 view projections.

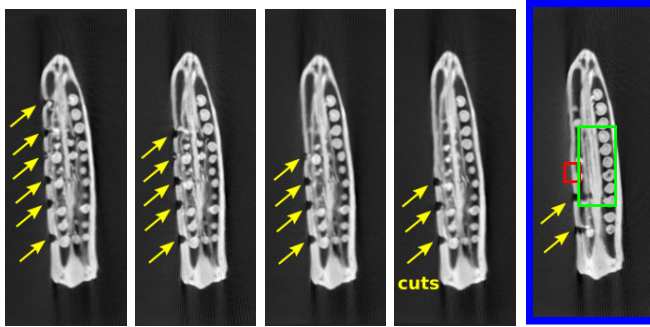


Fig. 3: Okra 3D dataset: One slice each from the scanned objects that are used as object-prior (the first four from left) and a slice from the test volume (extreme right). Notice the regions marked in red and green boxes; while all slices have deformities, the test has none.

Potato: This dataset consisted of four scans of the humble potato (Fig. 4). While the first scan was taken of the undistorted potato, subsequent scans were taken of the same specimen, each time after drilling a new hole halfway into the potato. Measurements from each scan consisted of real circular cone-beam projections from 900 views, each of size 150×150 . In our experiments, the first 3 volumes were used to build the object-prior and the last volume was used as the test. The ground truth consists of volumes of size $150 \times 150 \times 100$ reconstructed using FDK from the full set of 900 projection views.

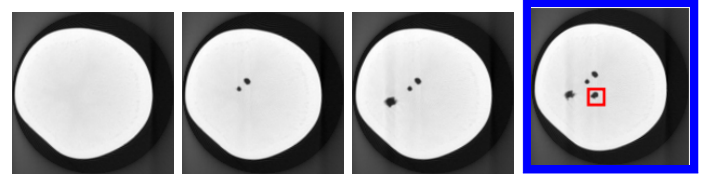


Fig. 4: Potato 3D dataset: One slice each from the previously scanned objects (the first three from left) and a slice from the test volume (extreme right). Notice the appearance of the fourth hole in the test slice.

Sprouts: This 3D dataset, which was also obtained at ANU, consists of six reconstructed volumes corresponding to six scans of an in-vivo sprout specimen imaged at its various stages of growth (Fig. 5). *In contrast to the scientific experiment performed for the case of the okra and potato where we introduced man-made defects, the changes here are purely the work of nature.* In our experiments, the first 5 volumes were used to build the object-prior and the last volume was used as the test. The ground truth consists of FDK reconstructed volumes of size $130 \times 130 \times 130$ from a set of 1800 view projections. For the test, cone-beam projections were generated from the test volume.

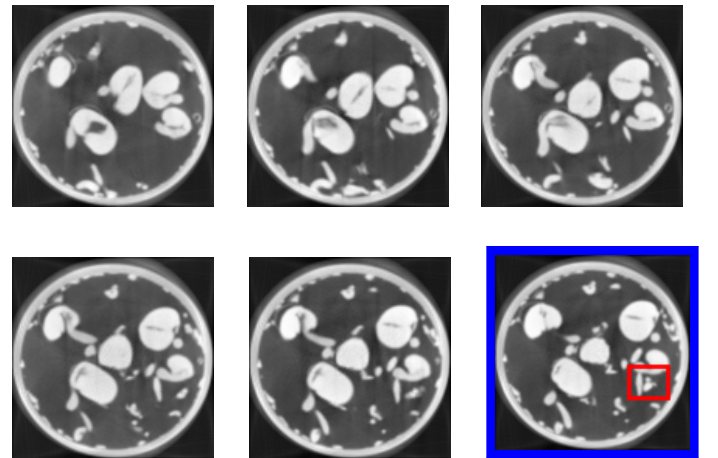


Fig. 5: Sprouts 3D dataset: One slice each from the previously scanned objects (the first five from left) and a slice from the test (extreme right). Notice the structure within the red box in the test that is different from all of the other images.

Liver: This data was sourced from Tata Memorial Cen-

tre [31] in Parel, Mumbai. This is the national comprehensive centre for the prevention, treatment, education and research in cancer, and is recognized as one of the leading cancer centres in India. The dataset (Fig. 6) from this longitudinal medical study consists of 8 scans taken at different stages of radio-frequency ablation study of a liver. In such a procedure [32], the physician inserts a thin needle-like probe into the organ. Repeated CT scans of the patient are acquired in order to track the movement of the needle and to ensure that it is reaching the appropriate target tumor. Once the needle hits the tumor, a high-frequency electric current is passed through the tip of the probe and this burns the malignant tumor (ablation). The aim of the scan at this ablation stage is to reveal accurate details of the changes within.

In our experiments, we generate parallel beam measurements from 2D slices from each of the 8 volumes. Note that all these 8 slices are located at the *same* index (slice number corresponding to the same depth) within each of the respective volumes. Observe (in Fig. 6) that the needle is seen in all of the first 7 slices and the effect of ablation is seen in the 8th slice.

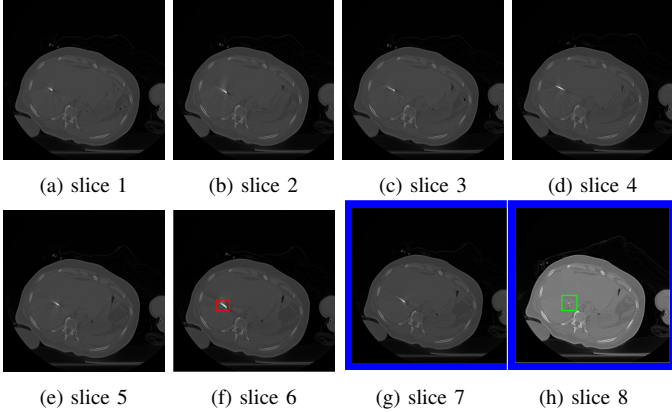


Fig. 6: Radio-frequency ablation dataset: One of the slices (512×512) from each of the 8 scan volumes of a longitudinal study dataset of the liver. Note that in volumes (a) through (g), the needle (shown in red in (f)) approaches the target tumor. (h) the organ after the ablation; this slice is displayed on a separate intensity scale to enable proper viewing of the region marked in green that shows the after-effects of ablating the tumor.

V. APPLICATION: RECONSTRUCTION FOR CT-GUIDED RADIO-ABLATION STUDY

Before diving into the details of the uniform and the spatially-varying prior methods, we first show how *both* the techniques can be applied to our advantage in a real-life medical longitudinal study. Here, our data consists of successive scans of the liver taken during a radio-frequency ablation procedure as described in Sec. IV. In this context, we classify the goal of any of our reconstruction techniques into two categories:

- 1) to track the position of the needle, and
- 2) to accurately observe the new changes when the needle touches the tumor,

while simultaneously reducing the sub-sampling artefacts. The choice of the number of measurement views and the type

of reconstruction – uniform or spatially-varying, is driven by the goal of the procedure. First, in order to track the needle, a very small number of views is sufficient because the needle has a very high attenuation coefficient when compared to that of the organs. We use the uniform prior reconstruction here to reduce the artefacts due to sub-sampling. The uniform method is fast and sufficient to track the position of the needle. Once the needle reaches the site of the tumor, we propose changing the imaging protocol to acquire measurements from a moderate number of views. This will enable us to get more information about the new changes. In addition, we then deploy the spatially-varying prior method in order to locate the regions of new changes and penalize any dominance of the prior in these regions. Regardless of the imaging protocol we use ('few' or 'moderate'), the number of views is smaller (atleast one-fifth) than the conventional number of views used in a standard hospital setting. To summarize, when our aim is

- **Tracking the needle**, we first choose slices 1-6 as our object-prior, and reconstruct slice 7 with the specific goal of tracking the needle and simultaneously reduce artefacts. Fig. 7 shows the reconstruction of slice 7 from its measurements from only 90 views. The reconstructions are quantitatively compared using SSIM.

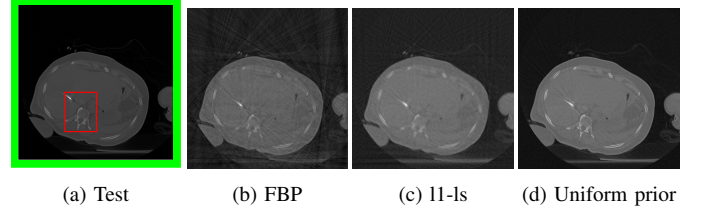


Fig. 7: **Goal: Track new changes.** Reconstruction of slice 7 ('test') of Fig. 6 from only 90 views, using (b) FBP and no prior resulting in streaks, SSIM=0.48 (c) 11-ls resulting in blurred bone structures (reasons discussed in Sec. 5 of our supplementary material [29]), SSIM=0.35 and (d) uniform prior (slices 1-6 of Fig. 6 are used as object-prior) resulting in clear bone structures with less streaks, SSIM=0.55. The region enclosed in red rectangle is our Region of Interest (RoI) as it contains both the new position of the needle and some background. All SSIM values are computed for this RoI.

- **Observing details of the ablation**, we choose slices 1-7 as our object-prior and reconstruct slice 8 from 120 views, i.e., a somewhat higher number of views this time. Fig. 8 shows the reconstructions of slice 8 by different methods.

We see that the spatially-varying prior reconstruction brings in the advantage of the prior without adversely affecting the reconstruction of new regions.

VI. UNIFORM PRIOR-BASED RECONSTRUCTION

Having presented the application, we first review the algorithm [33] for a uniform prior-based reconstruction since we are extending this algorithm to 3D reconstructions as part of this work. We first present the eigenspace-cum-CS prior-based reconstruction. To begin with, when an object is scanned multiple times, a set of high quality reconstructions (i.e., reconstructions from a dense set of projection views) may be chosen as object-prior for the reconstruction of future

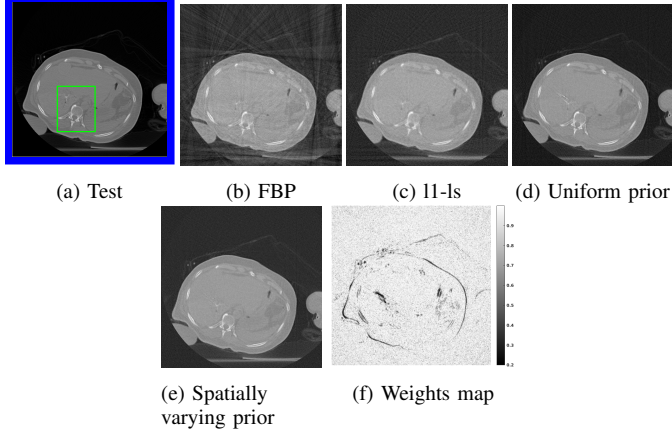


Fig. 8: Goal: Observe details of new changes. Reconstruction of slice 8 of Fig. 6 from 120 views, using (b) FBP with SSIM=0.50 (c) 11-ls with SSIM=0.46 and (d) uniform prior, with SSIM=0.51 (*notice dominance of the prior: a prominent residual shadow of the needle which was present in the object-prior, but not present in the test image*), and (e) spatially-varying prior with SSIM=0.56 (*notice that the dominance of the prior is significantly controlled*). The region enclosed in green rectangle is our RoI as it contains both the new position of the needle and some background. The SSIM is computed in this RoI. (f) shows the computed weights map (defined later in the paper) used for reconstruction. Darker intensities indicate lower weights to prior as these are the regions of new changes.

scan volumes, which in turn, may be scanned using far fewer measurements. The eigenspace E_{high} of the L previously scanned objects Q_1, Q_2, \dots, Q_L is pre-computed. Here, it is assumed that most of the test volume, barring the new changes, can be expressed as a sparse linear combination of the principal components (eigenvectors of the covariance matrix) obtained from a group of structurally similar volumes. Hence, the object-prior is represented by means of PCA. For the eigenspace to encompass a range of possible structures in the test slice, the object-prior must represent a wide structural range. Moreover, if these volumes are not aligned, then they must be first registered before computing the prior. The prior is built by computing the covariance matrix from the template set $\{Q_i\}_{i=1}^L$. The space spanned by the eigenvectors $\{V_k\}_{k=1}^{L-1}$ (eigenspace) of the covariance matrix is the object prior and is assumed to contain most of the test slice that is similar, but not necessarily identical to the object-prior. We use all of the $L-1$ orthogonal eigenvectors as a basis to represent the unknown test volume. Let μ denote the mean of the previously scanned objects, and α the unknown vector of eigen-coefficients of the test scan, of which α_k is the k^{th} element. Then, once the eigenspace is pre-computed, the test is reconstructed by minimizing the following cost function:

$$J_1(\theta, \alpha) = \|\mathcal{R}\mathbf{x} - \mathbf{y}\|_2^2 + \lambda_1 \|\theta\|_1 + \lambda_2 \|\mathbf{x} - (\mu + \sum_k V_k \alpha_k)\|_2^2. \quad (2)$$

Here, λ_1, λ_2 are tunable weights given to the sparsity and prior terms respectively. The unknowns θ and α are solved by alternately minimizing $J_\alpha(\theta)$ using a fixed α , and $J_\theta(\alpha)$

using the resultant θ , where

$$J_\alpha(\theta) \triangleq \|\mathcal{R}\mathbf{x} - \mathbf{y}\|_2^2 + \lambda_1 \|\theta\|_1 + \lambda_2 \|\mathbf{x} - (\mu + V\alpha)\|_2^2, \quad (3)$$

$$J_\theta(\alpha) \triangleq \|\mathbf{Y}\theta - (\mu + V\alpha)\|_2^2. \quad (4)$$

θ is solved for using the basis pursuit CS solver, (11-ls) [14]. Solving for α leads to the closed form update:

$$\alpha = V^T(\mathbf{Y}\theta - \mu). \quad (5)$$

The cost function described in Eq. 2 is biconvex and the convergence of this optimization is guaranteed by the monotone convergence theorem [34].

VII. RESULTS: RECONSTRUCTION BY UNIFORM PRIOR

The proposed method has been validated on new scans of biological specimens in a longitudinal setting.

1) Okra: The test volume was reconstructed from a partial set of 45 projections, i.e., 10% of the projection views from which ground truth was reconstructed. One of the slices of the reconstructed volumes is shown in Fig. 9. The SSIM values presented in Table I show that the presence of a uniform object prior significantly improves the overall reconstruction in comparison with the usage of sparsity prior alone. The selected 3D ground truth of template volumes, the test volume as well as the 3D reconstructions can be seen in the supplementary material [29].

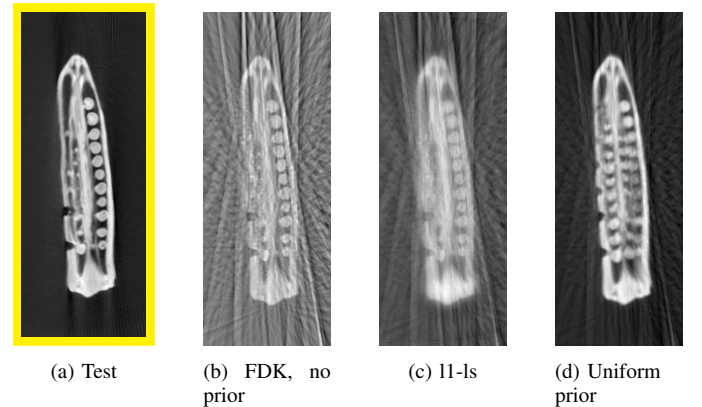


Fig. 9: 3D reconstruction of the okra from 10% projection views (b) has strong streak artefacts, (c) blurred (reasons discussed in Sec. 5 of our supplementary material [29]), (d) The prior enables better reconstruction. The reconstructed volumes can be viewed in the supplementary material [29].

TABLE I: SSIM of the full reconstructed okra volume by various methods. The SSIM of ground-truth (ideal reconstruction) is 1.

	FDK	11-ls	Uniform prior + 11-ls
full Volume	0.83	0.87	0.89

2) Sprouts: The test volume was reconstructed from partial set of 45 projections, i.e., 2.5% of the projection views from which ground truth was reconstructed. One of the slices of the reconstructed volumes is shown in Fig. 10. Table II shows the SSIM of the full reconstructed volumes. Here again, the presence of a uniform object prior significantly improves the

TABLE II: SSIM of the full reconstructed sprouts volume by various methods. The SSIM of ground-truth (ideal reconstruction) is 1.

	FDK	ll-ls	Uniform prior + ll-ls
Full volume	0.91	0.82	0.95

overall reconstruction in comparison with the usage of sparsity prior alone. The selected 3D ground truth of template volumes, the test volume as well as the 3D reconstructions can be seen in the supplementary material [29].

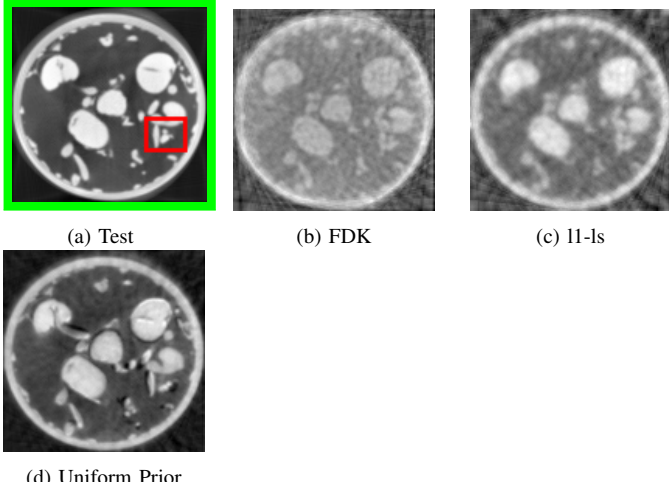


Fig. 10: 3D reconstruction of sprouts from 2.5% projection views (b, c) have poor details (d) no new information detected (the prior dominates as can be seen in the blue and red regions) and (e) new information detected in the regions of interest. The reconstructed volumes can be viewed in the supplementary material [29].

VIII. SPATIALLY-VARYING PRIOR-BASED RECONSTRUCTION

Although the uniform prior can be very useful in some circumstances, as was shown in Sec. V, it poses a limitation when we want accurate details of a portion of the new changes. While the uniform prior compensates very well for the possible artefacts due to sparse measurements, it may dominate the regions with new changes masking the signal, as was seen earlier in Fig. 8(d). Ideally, we will want to impose the prior only in the regions that are common between the test and object-prior. Our spatially-varying prior based reconstruction overcomes this limitation by minimizing the following cost function:

$$J_3(\boldsymbol{\theta}, \boldsymbol{\alpha}) = \|\mathcal{R}\mathbf{x} - \mathbf{y}\|_2^2 + \lambda_1 \|\boldsymbol{\theta}\|_1 + \lambda_2 \|\mathbf{W}(\mathbf{x} - (\boldsymbol{\mu} + \sum_k \mathbf{V}_k \boldsymbol{\alpha}_k))\|_2^2. \quad (6)$$

The key to our method is the discovery of a diagonal weights matrix \mathbf{W} , where W_{ii} contains the (non-negative) weight assigned to the i^{th} voxel of the prior. \mathbf{W} is first constructed using some preliminary reconstruction methods, following which Eq. 6 is used to obtain the final reconstruction. In regions of change in test data, we want lower weights for the prior when compared to regions that are similar to the prior.

Computation of weights matrix \mathbf{W} : Since the test is unknown to begin with, it is not possible to decipher the precise regions in \mathbf{x} that are different from all the previously scanned objects ('object-prior'). We start with X^{fdk} , the initial backprojection reconstruction of the test volume using FDK in an attempt to discover the difference between the object-prior and the test volume. Let \mathbf{V}_{high} be the eigenspace constructed from high-quality object-prior. However, the difference between X^{fdk} and its projection onto the eigenspace \mathbf{V}_{high} will detect the new regions along with many false positives (false new regions). This is because, X^{fdk} will contain many geometric-specific artefacts arising from sparse measurements (angle undersampling), which are absent in the high quality object-prior used to construct the eigenspace \mathbf{V}_{high} . To discover unwanted artefacts of the imaging geometry, in a counter-intuitive way, we generate *low quality* reconstruction of the object-prior as described below.

Algorithm to compute weights-map \mathbf{W} :

- 1) Perform a pilot reconstruction X^{fdk} of the test volume \mathbf{x} using FDK.
- 2) Compute low quality template volumes Y^{fdk} . We assume L previously scanned objects from which we build an eigenspace.
 - a) Generate simulated measurements \mathbf{y}_{Q_i} for every template Q_i , using the exact same projections views and imaging geometry with which the measurements \mathbf{y} of the test volume \mathbf{x} were acquired, and
 - b) Perform L preliminary FDK reconstructions of each of the L object-prior from \mathbf{y}_{Q_i} . Let this be denoted by $\{Y_i^{\text{fdk}}\}_{i=1}^L$.
- 3) Build eigenspace \mathbf{V}_{low} from $\{Y_i^{\text{fdk}}\}_{i=1}^L$. Let P^{fdk} denote projection of X^{fdk} onto \mathbf{V}_{low} . The difference between P^{fdk} and X^{fdk} will not contain false positives due to imaging geometry, but will have false positives due to artefacts that are specific to the reconstruction method used. To resolve this, perform steps 4 and 5.
- 4) Project with multiple methods.
 - a) Perform pilot reconstructions of the test using M different reconstruction algorithms like the CS [35], Algebraic Reconstruction Technique (ART) [36], Simultaneous Algebraic Reconstruction Technique (SART) [37] and Simultaneous Iterative Reconstruction Technique (SIRT) [38]. Let this set of pilot reconstructions be denoted as $X \triangleq \{X^j\}_{j=1}^M$ where j is an index for the reconstruction method, and $X^1 = X^{\text{fdk}}$.
 - b) From \mathbf{y}_{Q_i} , perform reconstructions of the template Q_i using the M different algorithms, for each of the L previously scanned objects. Let this set be denoted by $Y \triangleq \{Y_i^j\}_{j=1}^M \}_{i=1}^L$ where $Y_i^1 = Y_i^{\text{fdk}}$, $\forall i \in \{1, \dots, L\}$.
 - c) For each of the M algorithms (indexed by j), build an eigenspace $\mathbf{V}_{\text{low}}^j$ from $\{Y_1^j, Y_2^j, \dots, Y_L^j\}$.
 - d) Next, for each j , project X^j onto $\mathbf{V}_{\text{low}}^j$. Let this

projection be denoted by P^j . To reiterate, this captures those parts of the test volume that lie in the subspace V_{low}^j (i.e., are similar to the template reconstructions). The rest, i.e., new changes and their reconstruction method-dependent-artefacts, are not captured by this projection and need to be eliminated.

- 5) To remove all reconstruction method dependent false positives, we compute $\min_j(|X^j(x, y, z) - P^j(x, y, z)|)$. (The intuition for using the ‘min’ is provided in the paragraph immediately following step 6 of this procedure.)
- 6) Finally, the weight to prior for each voxel coordinate (x, y, z) is given by

$$\mathbf{W}_v(x, y, z) = (1 + k(\min_j |X^j(x, y, z) - P^j(x, y, z)|))^{-1} \quad (7)$$

Note that here $\mathbf{W}_v(x, y, z)$ represents the weight to the prior in the $(x, y, z)^{\text{th}}$ voxel. $\mathbf{W}_v(x, y, z)$ must be low whenever the preliminary test reconstruction $X^j(x, y, z)$ is different from its projection $P^j(x, y, z)$ onto the prior eigenspace, for every method $j \in \{1, \dots, M\}$. This is because it is unlikely that *every* algorithm would produce a significant artefact at a voxel, and hence we hypothesize that the large difference has arisen due to genuine structural changes. The parameter k decides the sensitivity of the weights to the difference $|X^j(x, y, z) - P^j(x, y, z)|$ and hence it depends on the size of the new regions we want to detect. We found that our final reconstruction results obtained by solving Eq. 6 were robust over a wide range of k values, as discussed in Sec. X.

Motivation for the use of multiple types of eigenspaces for the computation of weights:

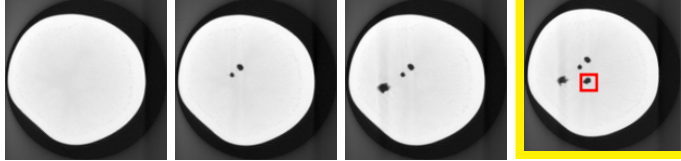


Fig. 11: Potato dataset: One slice each from the previously scanned objects (the first three from left) and a slice from the test volume (extreme right). Notice the appearance of the fourth hole in the test slice.

The changes and new structures present in the test data will generate different artifacts for different reconstruction techniques. These artifacts would not be captured by reconstructions of the object-prior since the underlying new changes and structures may be absent in all of the previously scanned objects. We aim to let the weights be independent of the type of artifact. Hence, we use a combination of different reconstruction techniques to generate different types of eigenspaces and combine information from all of them to compute weights. To illustrate the benefit of this method, we first performed 2D reconstruction of a test slice from the potato dataset. Fig. 11 shows the test and template slices. Fig. 12 shows the weights-maps generated using Eq. 7 by various

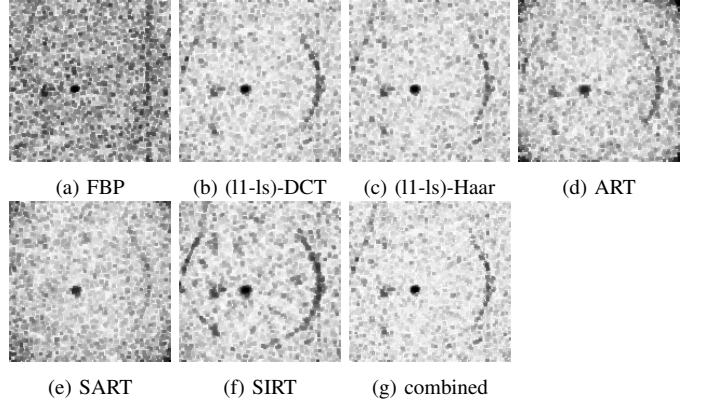


Fig. 12: Weights-maps (corresponding to the difference between pilot reconstruction of the image in the last sub-figure of Fig. 11 and its projection onto the eigenspace V_{low}) constructed using different reconstruction methods individually (a-f) and collectively (g) by fusing information from all reconstruction methods, as specified in Eq. 7. The weights-maps are different because the reconstruction artefacts of the new structures in test image will be different for every reconstruction method used, as seen in Fig. 13.

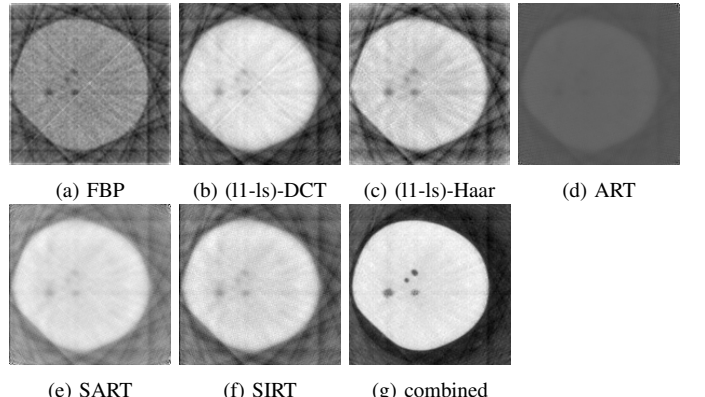


Fig. 13: (a)-(f):Different reconstructions of 11(d). The magnitude and sharpness of the artefacts is different for each method. (g) Spatially-Varying-prior method that combines weights-map information from all other methods. The SSIM of these reconstructions is shown in Table. III.

reconstruction methods. It can be seen that the weights are low in the region of the new change in test data. Because all the iterative methods are computationally expensive, we chose only FBP and (l1-ls)-DCT for computing weights-maps for all 3D reconstructions.

TABLE III: SSIM of the reconstructions shown in Fig. 13:(a)-(g). The SSIM of ground-truth (ideal reconstruction) is 1, and these are computed within the red RoI of the test image shown in Fig. 11d.

Fig. 13	(a)	(b)	(c)	(d)	(e)	(f)	(g)
red RoI	0.50	0.60	0.45	0.47	0.56	0.52	0.76

IX. RESULTS: RECONSTRUCTION BY SPATIALLY-VARYING PRIOR

The results below show the advantage of spatially-varying prior over uniform prior while reconstructing details of the new changes within the object.

1) *Okra*: The test volume was reconstructed from a partial set of 45 projections, i.e., 10% of the projection views from which ground truth was reconstructed. One of the slices from the reconstructed volumes is shown in Fig. 14. The red and green 3D ROI in the video and images show the regions where new changes are present. The zoomed-in images around the major region of change (red ROI) is shown in Fig. 15. As in the test, the reconstruction by spatially-varying method shows the absence of the deformity and better removal of sub-sampling artefacts when compared to FDK and 11-ls. This is also seen in the SSIM values in Table IV.

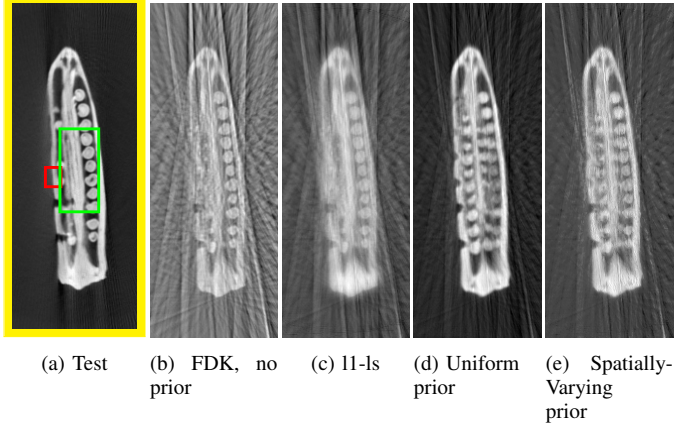


Fig. 14: 3D reconstruction of the okra from 10% projection views (b) has strong streak artefacts, (c) blurred, (d) no new information detected (prior dominates – the deformity from the prior shows up as a false positive) and (e) new information detected (no deformities corresponding to red and green regions) while simultaneously reducing streak artefacts. The reconstructed volumes can be viewed in the supplementary material [29].

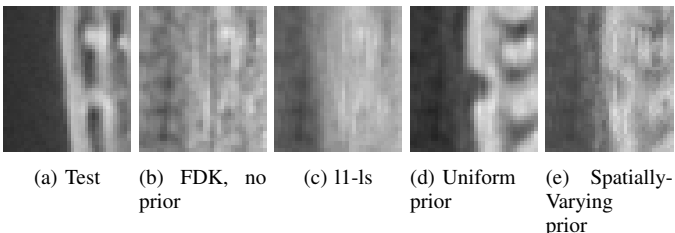


Fig. 15: Zoomed in portion corresponding to the red ROI of Fig. 14 for various methods (b) has strong streak artefacts, (c) blurred, (d) no new information detected (prior dominates – the deformity from the prior shows up as a false positive) and (e) new information detected (no deformities).

TABLE IV: SSIM of 3D ROI of reconstructed okra volumes from various methods. Each ROI spans 7 consecutive slices where the test is different from all of the previously scanned objects. The SSIM of ground-truth (ideal reconstruction) is 1.

	FDK	11-ls	Uniform prior + 11-ls	Spatially Varying prior + 11-ls
red ROI	0.74	0.84	0.85	0.88
green ROI	0.81	0.82	0.77	0.83

2) *Sprouts*: The test volume was reconstructed from partial set of 45 projections, i.e., 2.5% of the projection views from which ground truth was reconstructed. The selected 3D ground

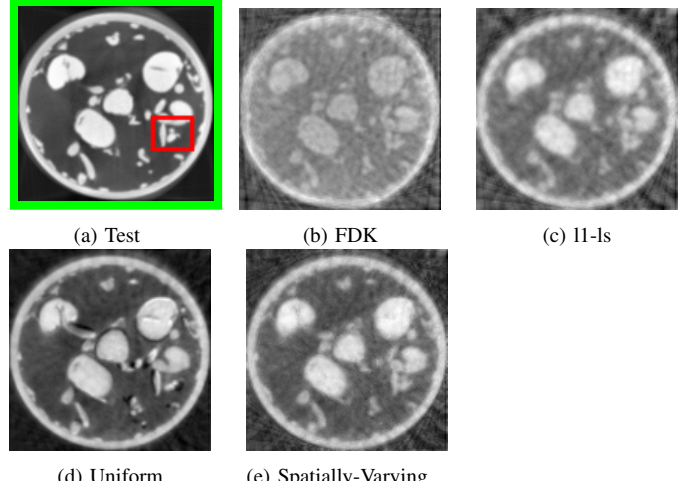


Fig. 16: 3D reconstruction of sprouts from 2.5% projection views (b, c) have poor details (d) no new information detected (the prior dominates as can be seen in the blue and red regions) and (e) new information detected in the regions of interest. The reconstructed volumes can be viewed in the supplementary material [29].

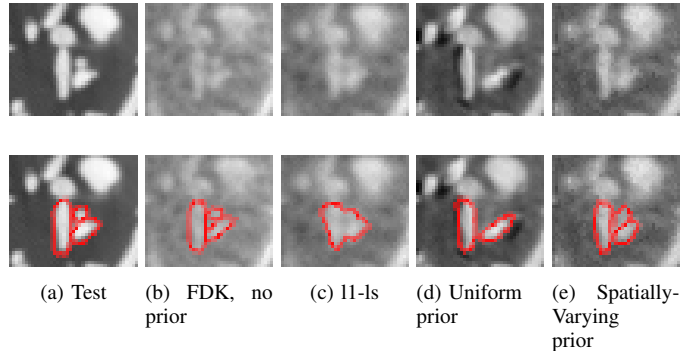


Fig. 17: Zoomed-in portion (41 x 36) containing the ROI of Fig. 16 for various methods. The images of the bottom row are the same as respective images of the top row, with regions marked additionally. (a) the test showing 3 distinct structures (in red here) (b) 3 structures recovered with poor contrast, (c) structures indistinguishable, (d) only two strong structures seen and (e) there is a hint of a third structure too with better contrast.

TABLE V: SSIM of 3D ROI of reconstructed sprouts volumes from various methods. The ROI spans 7 consecutive slices where the test is different from all of the previously scanned objects.

	FDK	11-ls	Uniform prior + 11-ls	Spatially Varying prior + 11-ls
red ROI	0.85	0.86	0.83	0.88

truth of template volumes, test volume, as well as the 3D reconstructions are shown in the supplementary material [29]. One of the slices of the reconstructed volumes and its zoomed-in ROI are shown in Figs. 16 and 17 respectively. For the sake of exposition, the red region of interest (ROI) has been culled out from 7 consecutive slices in the 3D volume to indicate new structures; other changes can be viewed in the video. Tables IV and V show the improvement in SSIM of the reconstructed new regions as compared to other methods.

X. DISCUSSION

In this section, we discuss the following: a) an alternate imaging and reconstruction protocol for longitudinal studies, b) results on homogeneous dataset, and (c) tuning of the parameters used.

A. An alternate imaging and reconstruction protocol

Earlier in Sec. V, we discussed that the imaging protocols fell under two categories depending on the final goal (tracking or observing details): very few-view imaging and moderate view imaging. In both cases, the templates used were of high-quality. However, in a realistic scenario, we may prefer to gradually increase from few-view to moderate views as the probe gradually approaches the tumor site. For the reconstruction of n^{th} slice i.e., slice imaged at time $t = n$, the few-view reconstructions of the previously acquired slices can be used as templates. However, the first scan must always be taken with large number of views because it acts as a reference template to start with. Table. VI summarizes this protocol for the dataset of Fig 6, and Fig. 18 shows the reconstructions when this realistic protocol is used.

TABLE VI: Suggested multi-step imaging protocol for the CT-guided radio-frequency ablation dataset of Fig 6. The number of views is gradually increased as the probe approaches the tumor site. Only the first scan is taken with large number of views to act as a reference template. The few-view reconstructions of a slice acts as the object-prior for the reconstruction of slice being imaged at next time instant.

Slice being imaged at time t	Probe distance from tumor or ablation stage	Number of imaging views	Reconstruction protocol: type of prior
Slice $t=1$	Very far from tumor	360	l1-ls
Slice $t=2$	Sufficiently far from tumor	40	Uniform
Slice $t=3$	Far from tumor	50	Uniform
Slice $t=4$	Near tumor	60	Uniform
Slice $t=5$	Sufficiently near tumor	70	Uniform
Slice $t=6$	Very near tumor	80	Uniform
Slice $t=7$	Very near tumor	90	Uniform
Slice $t=8$	During, after ablation	120	Spatially-Varying

B. Reconstruction of homogeneous data

TABLE VII: SSIM of 3D reconstructed potato volumes from various methods. Each ROI spans 7 consecutive slices where the test is different from all of the previously scanned objects. In this dataset alone, the new changes are in a homogeneous background. Hence, the FDK performs the best when the ROI alone is considered. However, it fails when the entire volume is considered due to the prominent streaky artefacts.

	ground truth	FDK	l1-ls	Uniform prior + l1-ls	Spatially-Varying prior + l1-ls
red ROI volume	1 (ideal)	0.94	0.88	0.71	0.85
green ROI volume	1 (ideal)	0.92	0.91	0.87	0.88
cyan ROI volume	1 (ideal)	0.88	0.94	0.92	0.89
full volume	1 (ideal)	0.74	0.81	0.86	0.86

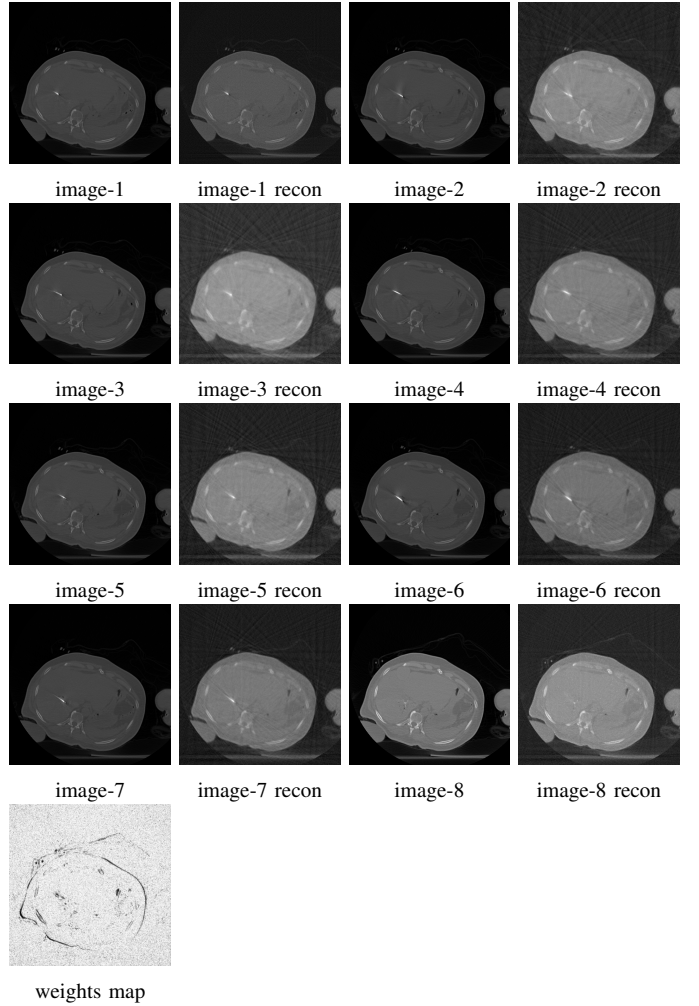


Fig. 18: Reconstructions (referred as ‘recon’) of all slices of of Fig. 6 using the suggested protocol in Table. VI. The last image is the weights map corresponding to the reconstruction of image-8. The new changes in the tumor site is picked up by the weights map.

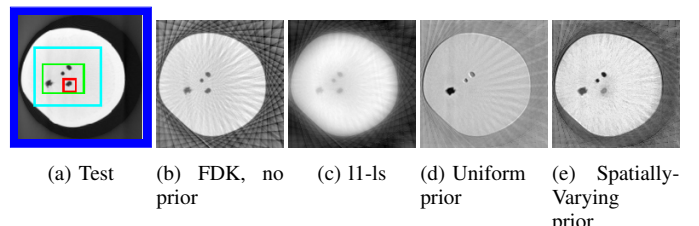


Fig. 19: Slice-A from 3D reconstruction of the potato with 5% projection views—(b) has strong streak artefacts with unclear shadow of the potato, (c) largely blurred, (d) no new information detected (prior dominates) and (e) new information detected while simultaneously reducing streak artefacts. The reconstructed volumes can be viewed in the supplementary material [29].

While the design of the weights map in the proposed algorithm aims to combine the best of information from both the current measurements and the prior, we found FDK to be preferable when the test object has a simple, homogeneous structure without intricate details. One such dataset is the Potato dataset (described in Sec. IV). The test volume was reconstructed using measurements from 45 projection views,

i.e., 5% of the projection views from which ground truth was reconstructed. The selected 3D ground truth of template volumes, test volume, as well as the 3D reconstructions are shown in the supplementary material [29]. Fig. 19 shows a slice from the reconstructed 3D volume. We observe that our method reconstructs new structures while simultaneously reducing streak artefacts. Table VII shows the Structure Similarity Index (SSIM) of the reconstructed new regions using various methods. We observe that FDK performs very well for smaller ROI; as the ROIs get bigger, the FDK reconstructions have poor SSIM due to strong subsampling artefacts. In contrast, the results from 11-Is and our method progressively improve when compared to FDK as the ROIs get bigger. In practice, the ROI is not known in advance and hence, one may choose FDK for the case of simple, homogeneous dataset with smaller ROI, and prefer spatially-varying prior-based reconstruction when the dataset is complex and ROIs are larger.

C. Tuning of parameters

λ_1 was tuned to maximize SSIM of the whole reconstructed test volume for 11-Is reconstruction of each dataset. This value was retained for uniform and spatially-varying prior-based reconstruction as well. The value of λ_2 largely depends on the amount of artefacts we aim to remove by using prior at the cost of their dominance in the new regions. This value was chosen to lie between 0 – 1 for our datasets. Finally, the hyper-parameter k defines the sensitivity of the weights map to the difference between the test image and the prior (projection of test onto the space of object-prior). When $k = 0$, our method converges to the uniform prior method. As k increases, the weights map starts capturing the new changes in the test, at the cost of detecting a few false positives i.e., false new changes. In other words, as the weights map becomes more sensitive to the difference between the test and object-prior, it becomes more noisy. In order to visualize the effect of the hyper-parameter k , we performed 2D reconstructions of okra dataset for different values of k . Fig. 20 shows the weights map obtained for each of the k values. We estimate an approximate choice for the optimal value of k by treating one of the object-prior as test and reconstructing it. We also note that although the weights map is heavily influenced by k , the final reconstructions are stable for large variations in k , as seen in Fig. 21. Alternatively, in cases where one wishes to completely avoid the use of this hyper-parameter, one can construct a binary weights-map using a learning based method described in the supplementary material [29].

XI. CONCLUSIONS

This work deals with the effective use of priors for tomographic reconstruction in longitudinal studies. We show that we can either use the uniform prior method or the spatially-varying prior method to our advantage, depending on our goal. We establish the context under which these methods can be used, as outlined in Fig. 2. When we wish to approximately know the location of new changes, we apply a uniform prior because it is sufficient for the task at hand. We also choose a smaller number of views in order to reduce radiation. In

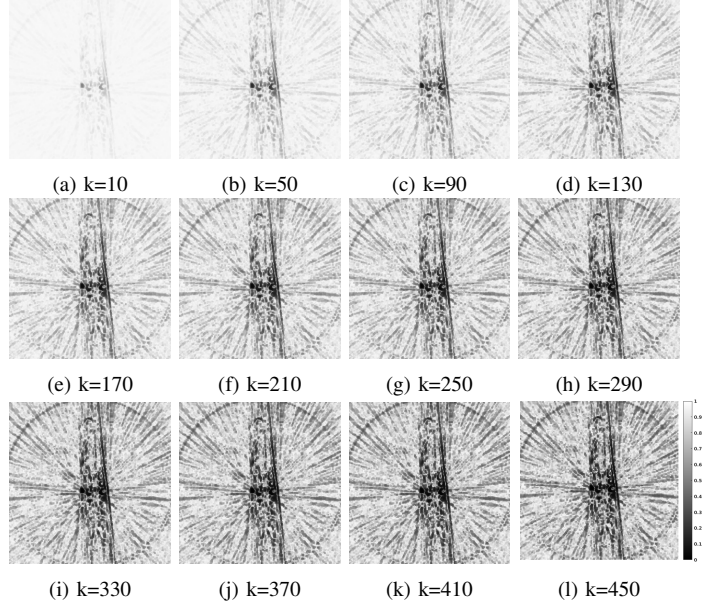


Fig. 20: Different weights-maps for okra reconstruction. Low intensity denotes regions of new changes in test.

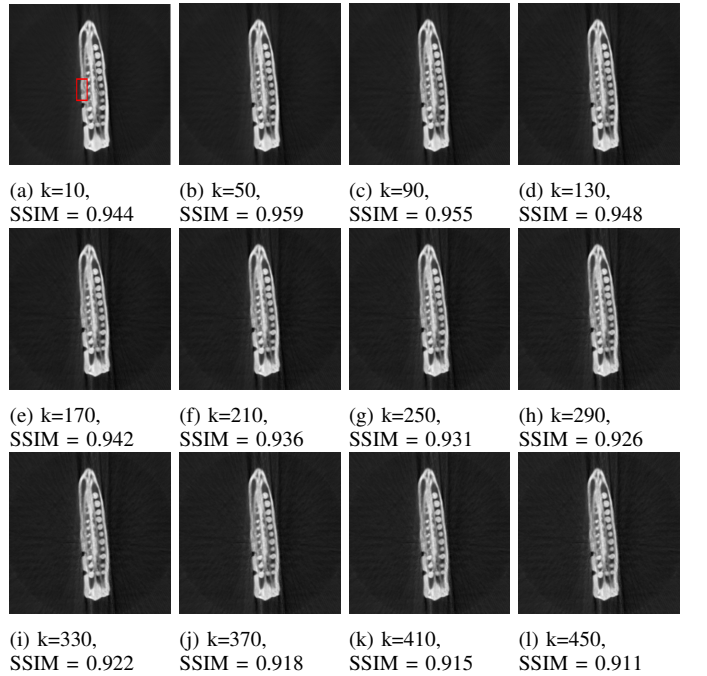


Fig. 21: 2D reconstructions showing stable reconstructions for large variations in k . The SSIM values for all images are computed within the red ROI (shown in (a)), the region where the test is different from all of the previously scanned objects.

addition, we show that when our goal shifts to observing the details of the new changes accurately, we acquire projections from a moderate number of views in order to capture more information. We further combine this with the somewhat slower but more accurate technique of reconstruction—the spatially-varying prior-based method. This method ensures that the reconstruction of localized new information in the data is not affected by the priors. We have thus improved the state of the art by detecting these regions of change and assigning

low prior weights wherever necessary. The probability of presence of a ‘new region’ is enhanced considerably by a novel combination of different reconstruction techniques. We have validated our technique on medical 2D and real, biological 3D datasets for longitudinal studies. The method is also largely robust to the number of previously scanned objects used. We urge the reader to see the videos of reconstructed volumes in the supplementary material [29].

XII. ACKNOWLEDGEMENT

We are grateful to Dr. Andrew Kingston for facilitating data collection at the Australian National University. AR gratefully acknowledges IITB Seed-grant 14IRCCSG012, as well as NVIDIA Corporation for the generous donation of a Titan-X GPU card, which was essential for computing 3D reconstructions for the research reported here. We also thank Dr. Akshay Baheti for providing us with medical data from Tata Memorial Hospital, Mumbai.

REFERENCES

- [1] X. Yang, V. De Andrade, W. Scullin, E. L. Dyer, N. Kasthuri, F. De Carlo, and D. Gürsoy, “Low-dose X-ray tomography through a deep convolutional neural network,” *Scientific Reports*, vol. 8, no. 1, 2018.
- [2] L. Fu *et al.*, “Comparison between pre-log and post-log statistical models in ultra-low-dose CT reconstruction,” *IEEE transactions on medical imaging*, vol. 36, no. 3, pp. 707 – 720, 2016.
- [3] Q. Xie, D. Zeng, Q. Zhao, D. Meng, Z. Xu, Z. Liang, and J. Ma, “Robust low-dose CT sinogram preprocessing via exploiting noise-generating mechanism,” *IEEE Transactions on Medical Imaging*, vol. 36, no. 12, pp. 2487–2498, Dec 2017.
- [4] P. Gopal, S. Chandran, I. Svalbe, and A. Rajwade, “Low radiation tomographic reconstruction with and without template information,” *Signal Processing*, vol. 175, p. 107582, 2020.
- [5] A. M. Kingston, G. R. Myers, S. J. Latham, B. Recur, H. Li, and A. P. Sheppard, “Space-filling X-ray source trajectories for efficient scanning in large-angle cone-beam computed tomography,” *IEEE Transactions on Computational Imaging*, vol. 4, no. 3, pp. 447–458, Sep. 2018.
- [6] A. Cazasnovas, S. Sevestre, F. Buyens, and F. Peyrin, “Statistical content-adapted sampling (SCAS) for 3D computed tomography,” *Computers in Biology and Medicine*, vol. 92, pp. 9 – 21, 2018.
- [7] O. Barkan, J. Weill, S. Dekel, and A. Averbuch, “A mathematical model for adaptive computed tomography sensing,” *IEEE Transactions on Computational Imaging*, vol. 3, no. 4, pp. 551–565, Dec 2017.
- [8] A. Fischer, T. Lasser, M. Schrapp, J. Stephan, and P. B. Noël, “Object specific trajectory optimization for industrial X-ray computed tomography,” *Scientific Reports*, vol. 6, no. 19135, Jan 2016.
- [9] A. Dabrowski, K. J. Batenburg, and J. Sijbers, “Dynamic angle selection in X-ray computed tomography,” *Nuclear Instruments and Methods in Physics Research Section B: Beam Interactions with Materials and Atoms*, vol. 324, pp. 17 – 24, 2014, 1st International Conference on Tomography of Materials and Structures.
- [10] L. L. Geyer, U. J. Schoepf, F. G. Meinel, J. W. Nance, G. Bastarrika, J. A. Leipsic, N. S. Paul, M. Rengo, A. Laghi, and C. N. De Cecco, “State of the art: Iterative CT reconstruction techniques,” *Radiology*, vol. 276, no. 2, pp. 339–357, 2015.
- [11] K. Kilic, G. Erbas, M. Guryildirim, M. Arac, E. Ilgit, and B. Coskun, “Lowering the dose in head CT using adaptive statistical iterative reconstruction,” *American Journal of Neuroradiology*, vol. 32, no. 9, pp. 1578–1582, 2011.
- [12] D. Donoho, “Compressed sensing,” *IEEE Transactions on Information Theory*, vol. 52, no. 4, pp. 1289–1306, April 2006.
- [13] E. Candès and M. Wakin, “An introduction to compressive sampling,” *IEEE Signal Proc. Mag.*, vol. 25, no. 2, pp. 21–30, March 2008.
- [14] K. Koh, S.-J. Kim, and S. Boyd, “l1-ls: Simple matlab solver for l1-regularized least squares problems,” https://stanford.edu/~boyd/l1_ls/, last viewed-July, 2016.
- [15] E. A. Rashed, M. al Shatouri, and H. Kudo, “Sparsity-constrained three-dimensional image reconstruction for C-arm angiography,” *Computers in Biology and Medicine*, vol. 62, pp. 141 – 153, 2015.
- [16] L. Liu, W. Lin, and M. Jin, “Reconstruction of sparse-view X-ray computed tomography using adaptive iterative algorithms,” *Computers in Biology and Medicine*, vol. 56, pp. 97 – 106, 2015.
- [17] A. G. Polak, J. Mroczka, and D. Wysoczański, “Tomographic image reconstruction via estimation of sparse unidirectional gradients,” *Computers in Biology and Medicine*, vol. 81, pp. 93 – 105, 2017.
- [18] G.-H. Chen, J. Tang, and S. Leng, “Prior image constrained compressed sensing (PICCS): A method to accurately reconstruct dynamic CT images from highly undersampled projection data sets,” *Medical Physics*, vol. 35, no. 2, pp. 660–663, 2008.
- [19] J. W. Stayman, H. Dang, Y. Ding, and J. H. Siewersden, “PIRPLE: A penalized-likelihood framework for incorporation of prior images in CT reconstruction,” *Physics in medicine and biology*, vol. 58, no. 21, pp. 7563–82, Nov 2013.
- [20] K. Ruymbeek and W. Vanroose, “Algorithm for the reconstruction of dynamic objects in CT-scanning using optical flow,” *Journal of Computational and Applied Mathematics*, vol. 367, p. 112459, 2020.
- [21] V. V. Nieuwenhove, “Model-based reconstruction algorithms for dynamic X-ray CT,” Ph.D. dissertation, University of Antwerp, 2017.
- [22] D. Kazantsev, W. M. Thompson, W. R. B. Lionheart, G. V. Eydohoven, A. P. Kaestner, K. J. Dobson, P. J. Withers, and P. D. Lee, “4D-CT reconstruction with unified spatial-temporal patch-based regularization,” p. 447, 2015.
- [23] G. Van Eydohoven, K. J. Batenburg, D. Kazantsev, V. Van Nieuwenhove, P. D. Lee, K. J. Dobson, and J. Sijbers, “An iterative CT reconstruction algorithm for fast fluid flow imaging,” *IEEE Transactions on Image Processing*, vol. 24, no. 11, pp. 4446–4458, 2015.
- [24] M. Heyndrickx, T. D. Schryver, M. Dierick, M. Boone, T. Bultreys, V. Cnudde, and L. V. Hoorebeke, “Improving the reconstruction of dynamic processes by including prior knowledge,” *HD-Tomo-Days, Abstracts.*, 2016.
- [25] Z. S. Hao Gao, Jian-Feng Cai and H. Zhao, “Robust principal component analysis-based four-dimensional computed tomography,” *Physics in Medicine and Biology*, vol. 56, no. 11, pp. 3181–98, Jun 7 2011.
- [26] V. E. G. B. KJ, and S. J., “Region-based iterative reconstruction of structurally changing objects in CT,” *IEEE Trans Image Process.*, vol. 23, no. 2, pp. 909–919, 2014.
- [27] A. Pourmorteza, H. Dang, J. H. Siewersden, and J. W. Stayman, “Reconstruction of difference using prior images and a penalized-likelihood framework,” *International Meeting on Fully Three-Dimensional Image Reconstruction in Radiology and Nuclear Medicine*, p. 252–257, 2015.
- [28] J. Lee, J. W. Stayman, Y. Otake, S. Schafer, W. Zbijewski, A. J. Khanna, J. L. Prince, and J. H. Siewersden, “Volume-of-change cone-beam CT for image-guided surgery,” pp. 4969–89, Aug 2012.
- [29] Supplemental material for ‘Eliminating object prior-bias from sparse-projection tomographic reconstructions’, “in Dropbox,” <https://www.dropbox.com/sh/sn9mvhym3sv4pj/AABLmnvlvRBeBQj-0miSn73Ba?dl=0>, Including video reconstruction results.
- [30] L. Feldkamp, L. C. Davis, and J. Kress, “Practical cone-beam algorithm,” *J. Opt. Soc. Am.*, vol. 1, pp. 612–619, 01 1984.
- [31] “Tata Memorial Centre,” https://en.wikipedia.org/wiki/Tata_Memorial_Centre, Wikipedia.
- [32] J. Dong, W. Li, Q. Zeng, S. Li, X. Gong, L. Shen, S. Mao, A. Dong, and P. Wu, “CT-guided percutaneous step-by-step radiofrequency ablation for the treatment of carcinoma in the caudate lobe,” *Medicine*, vol. 94, no. 39, 2015.
- [33] P. Gopal, R. Chaudhry, S. Chandran, I. Svalbe, and A. Rajwade, “Tomographic reconstruction using global statistical priors,” in *DICTA*, Sydney, Nov. 2017.
- [34] R. Meyer, “Sufficient conditions for the convergence of monotonic mathematical programming algorithms,” *Journal of Computer and System Sciences*, vol. 12, no. 1, pp. 108 – 121, 1976.
- [35] R. Tibshirani, “Regression shrinkage and selection via the Lasso,” *Journal of the Royal Statistical Society. Series B (Methodological)*, vol. 58, no. 1, pp. 267–288, 1996.
- [36] R. Gordon, R. Bender, and G. T. Herman, “Algebraic reconstruction techniques (ART) for three-dimensional electron microscopy and X-ray photography,” *Theoretical Biology*, vol. 29, no. 3, pp. 471–481, Dec 1970.
- [37] A. Andersen and A. Kak, “Simultaneous algebraic reconstruction technique (SART): A superior implementation of the ART algorithm,” *Ultrasonic Imaging*, vol. 6, no. 1, pp. 81 – 94, 1984.
- [38] P. Gilbert, “Iterative methods for the three-dimensional reconstruction of an object from projections,” *Journal of Theoretical Biology*, vol. 36, no. 1, pp. 105 – 117, 1972.